

The Influence of Physico-Chemical Properties of Bare Titania Powders Obtained from Various Synthesis Routes on Their Photo-Electrochemical Performance

T. Denaro¹, V. Baglio¹, M. Girolamo¹, G. Neri², F. Deorsola³, R. Ornelas⁴, F. Matteucci⁴,
V. Antonucci¹, A.S. Arico^{1,*}

¹ CNR-ITAE Institute, Via Salita S. Lucia sopra Contesse,5- 98126- Messina, Italy

² Dipartimento di Chimica Industriale e Ingegneria dei Materiali, University of Messina, 98166
Messina, ITALY

³ Politecnico di Torino, Dipartimento di Scienza dei Materiali e Ingegneria Chimica, C.so Duca degli
Abruzzi, Torino, Italy

⁴ Tozzi Renewable Energy, Mezzano, Ravenna, Italy

*E-mail: arico@itae.cnr.it

Received: 15 January 2012 / *Accepted:* 6 February 2012 / *Published:* 1 March 2012

Titania nanopowders prepared by different chemical routes as well as commercially available were investigated in terms of structure, chemistry, morphology, surface and optical properties by using various physical-chemical characterization techniques; these properties were related to their photo-electrochemical behaviour in a photo-electrolysis half-cell. Bare powders were used as photo-anodes without any doping treatment or addition of surface promoters and the photocurrent associated to the oxygen evolution rate was determined. This approach appears to provide suitable information about the powder quality for photo-electrochemical applications in the absence of any other modification or treatment. The investigated preparation procedures included sol-gel and combustion synthesis. Most of the powders showed an organic residue and the presence of contaminants both in the bulk and surface even if at a small level; moreover, only a few formulations showed a pure anatase phase. The highest photocurrent was obtained for the P25 commercial powder as a compromise of good chemical purity i.e. low occurrence of impurities acting as recombination or trapping centers for the photogenerated carriers and appropriate surface area/crystallite size characteristics associated with a suitable number of surface sites promoting the oxygen evolution under illumination. Good bulk and surface chemical purity, suitable surface area, proper particle size and appropriate morphology are among the most relevant properties that influence the photo-electrochemical behaviour.

Keywords: TiO₂; photoelectrolysis; physico-chemical properties; photoelectrochemical properties.

1. INTRODUCTION

The energy demand is increasing worldwide causing various concerns for the political and economic stability implications as well as for the significant environmental issues [1]. These problems may be addressed by achieving an abundant supply of clean energy from renewable sources. The increasing use of carbon-free energy sources that can meet a significant portion of societal demands appears as one of the major scientific challenges of the next decades [2-3]. It is well established that sun-light may become the most appropriate source of energy since the solar flux striking the earth corresponds to about 10^4 times the average global request of energy. Sunlight is readily available and it may allow a decentralised production of electric power or clean fuels such as hydrogen that may be utilised as an energy vector. While several technologies have been developed to convert solar energy efficiently, they are not yet economically competitive with respect to the combustion of fossil fuels [3]. Thus, cost-effective components and conversion processes need to be developed to provide a solution to the energy and environmental issues.

Recently, these aspects have been addressed by the development of alternative low-cost photovoltaic conversion devices such as Dye Sensitized Solar Cells (DSSC), or novel photoelectrochemical routes (e.g. tandem cells) for hydrogen production from solar light [4-16]. Both approaches make use of nanosized polycrystalline TiO_2 as one of the main components of these technologies. DSSCs comprise a nanoporous semiconducting photo-electrode made of sintered TiO_2 nanoparticles containing adsorbed dye molecules (e.g. a metal bipyridyl complex) [4]. Upon photo-excitation, the dye molecules generate electrons and holes and inject the electrons into the TiO_2 semiconductors. The excited dye cations are reduced to the neutral ground state by a redox couple in a liquid electrolyte (iodide/triiodide dissolved in an organic solvent). The triiodide to iodide cycle is completed by drawing electrons from the counter electrode. Because of the simplicity of the device and the low cost of TiO_2 , DSSCs display a great potential for large-scale applications [4, 9-16]. DSSCs have shown conversion efficiencies better than 10% and low degradation during long-term operation [6-8].

The dye molecules have strong optical absorbance in the visible light range whereas the function of the TiO_2 layer is to form the space charge region for current collection. A nanocrystalline structure for the TiO_2 semiconductor is critical since large surface area and small size of the crystals are required to anchor a large amount of dye molecules on the semiconductor surfaces; the electrons injected in the conduction band need to be effectively transferred before they are subjected to recombination phenomena with photogenerated holes by bulk or surface defects as well as grain boundaries.

A tandem cell consists of a photo-electrolysis cell in series to a DSSC device [5]. A semiconductor photoanode with large energy gap and appropriate matching with the electronic levels associated to the redox couples involved in water splitting is necessary for the electrolysis cell. Generally, O_2 evolution occurs at the photoanode whereas H_2 evolution occurs at the cathode (usually a thin transparent and ultra-low loading Pt layer). Thus, the photoelectrolysis cell absorbs mainly the UV portion of the solar spectrum whereas most of the visible energy reaches the DSSC cell and is converted into electricity that can be used to help water splitting in the photoelectrolysis cell [5].

TiO₂ has the proper characteristics and suitable electronic band structure to be used as photoanode for oxygen evolution in the photoelectrolysis cell [5, 17]. TiO₂ finds a widespread application also in photocatalysis, photo-electrochromics and sensors [18-22]. In all these applications, the electro-catalytic properties of titanium dioxide depend strongly on the processes occurring at the interface between the semiconductor surface and the surrounding medium. As an example, the photoelectrochemical process involving a charge transfer mediator occurs when the surface of the TiO₂ photo-anode is in direct contact with the liquid electrolyte. The semiconductor/liquid electrolyte interface plays an important role in determining an efficient water photo-electrolysis process [17]. In this perspective, a proper knowledge of the different semiconductor properties including its surface characteristics is important to predict its behaviour in all the above mentioned processes.

The performance of the photoelectrochemical, photo-electrochromic, sensor devices depends on several key components of the cells. In this regard, the properties of TiO₂ used in such devices are often investigated with the semiconductor in its final form i.e. sintered, doped, impregnated with the dye etc. Whereas, it would be worth of interest to investigate the material also in the bare form since most of these applications require similar properties for the semiconductor. As an example, a DSSC is a very complex device and the contribution of Titania to the overall cell performance is difficult to be determined [23]. An ex-situ screening method addressing structural and morphological properties only may be not sufficient whereas a photo-electrolysis half cell may allow to investigate and compare differently prepared materials with reference to the TiO₂-electrode/electrolyte interface processes. This approach may allow to deconvolute the role of bare Titania from other effects such as sintering level, doping, dye modifications that affect the photoelectrochemical behaviour. If half-cell photoelectrolysis tests are combined to a proper physico-chemical analysis of the relevant powder characteristics, these studies may represent a rapid screening method for TiO₂ application in photocatalysis.

The aim of this work is thus concerning with both physico-chemical and electrochemical characterizations of several TiO₂ semiconductors with different properties as screening approach for various applications including photoelectrochemistry. The water splitting properties were considered as a simple and useful indication of the semiconducting characteristics for applications involving a semiconductor-electrolyte interface. Several excellent reviews and reports on the preparation and properties of TiO₂ nanomaterials have been published recently [18, 22]. We have essentially focused our analysis on four different TiO₂ semiconductor powders. Two of them, TiO₂ Degussa P25 and TiO₂ Riedel-Hanover, were commercial powders while the other two were prepared in the laboratory, TiO₂ (T-37) and TiO₂ (TO), using sol-gel and gel-combustion synthesis, respectively.

2. EXPERIMENTAL DETAILS

2.1 Preparation and physicochemical characterization

The two commercial TiO₂ powders, Degussa P25 and TiO₂ Riedel-Hanover thereafter indicated simply as P25 and R-H were selected on the basis of the different particle size characteristics

indicated by the supplier. The T-37 Titania was prepared at University of Messina by a sol-gel synthesis. As well known, the sol-gel is a wet chemical method based on hydrolysis and condensation reactions of inorganic or alkoxide precursors, widely employed for its ability to achieve the low temperature preparation of gels suitable for deposition from the liquid phase and successive conversion into metal oxides networks by thermal treatment. Titania nanoparticles were thus obtained by precipitation in hydrothermal condition from mixed isopropanol/water solutions. Titanium isopropoxide (TiPT) was chosen as precursor instead of TiCl_4 , since the lower reactivity of the former enables the synthesis to be carried out without controlled atmosphere [24]. 2 mL of the TiPT (97%, supplied by Aldrich) were slowly added to 10 ml of 2 M ice-cold aqueous HCl solution, which was constantly stirred in a 50-mL volumetric flask. The acidity was needed to minimize the generation of orthotitanic acid $\text{Ti}(\text{OH})_4$, and to avoid any uncontrolled precipitation during the dissolution of TiPT in the aqueous solution. 60 mg of hydroxypropyl cellulose (HPC) and 20 mL of isopropanol (99%, Aldrich) were added after the solution became clear; it was kept under reflux at 100°C for 24 h to allow for a complete precipitation of nanoparticles. The suspension was thus rapidly cooled to room temperature and neutralized with NH_4OH 4 M to stabilize the nanoparticles.

TiO_2 TO was prepared by gel combustion synthesis at Politecnico di Torino. The gel combustion synthesis combines chemical gelation and combustion processes. The gel is formed from an aqueous solution containing the metal precursor and an organic fuel. An exothermic redox reaction is thermally induced between the metal precursor and the organic substance, giving rise to very porous and softly agglomerated powders. The process allows to enhance the control of homogeneity and stoichiometry of the prepared powders; it also permits to obtain metal oxide nanopowders in an extreme simple and rapid way [25]. TiO_2 nanopowders were prepared starting from titanium isopropoxide (Fluka), hydrogen peroxide (Fluka, 35%) and isopropanol (Aldrich, 99+%). Titanium isopropoxide was mixed with isopropanol. Hydrogen peroxide was added drop by drop in the continuously stirred solution. The reaction was supposed to be divided into two contemporary steps: the hydrolysis of Ti isopropoxide, causing the formation of titanium hydroxide (orthotitanic acid) $\text{Ti}(\text{OH})_4$ precipitate, and the oxidation of $\text{Ti}(\text{OH})_4$ precipitates developing titanium peroxy-complex, assumed to be in the form $\text{Ti}(\text{OOH})_4$, with remarkable release of gases and temperature increase until 80°C [26]. After drying the TiO_2 -containing gel, the products obtained were ground in a mortar and the powders were treated at 300°C for 1 h.

Several physical-chemical analyses were carried out to investigate structural, morphology and surface characteristics of the powders. In particular, bulk characterization of the powders was carried out by X-ray fluorescence (chemical) and X-ray diffraction (structural). The weight losses with the temperature and anatase-rutile phase transition was studied by Thermal gravimetry (TGA) and Differential scanning calorimetry (DSC). CHNS elemental analysis was carried out for a proper determination of light elements such as carbon, hydrogen, nitrogen and sulphur content in the materials. Surface area, pore distributions and pore volumes were investigated by BET analysis. Surface characterization was carried out by X-ray photoelectron spectroscopy (XPS). Morphological characteristics were observed by Transmission electron microscopy (TEM) measurements. Optical characterization for TiO_2 based photo-electrodes was performed by UV-Vis-NIR spectrophotometry.

The following instrumentation/methodology was used. X-ray Fluorescence analysis of the powders was carried out by a Bruker AXS S4 Explorer spectrometer operating at a power of 1 kW and equipped with a Rh X-ray source, a LiF crystal analyzer and a 0.12° divergence collimator. The CHNS analysis was carried out in a Flash EA 1112 Automatic Elemental Analyzer. Structural characterization of TiO₂ powders was performed using a Panalytical X'Pert powder diffractometer with CuK α radiation equipped with an automatic peak search program. The diffraction patterns were fitted to JCPDS (Joint Committee on Powder Diffraction Standards) and the crystallite size were calculated from peak broadening using the Debye-Sherrer method. XPS analysis was carried out with a PHI 5800-1 spectrometer. Surface area, pore size distribution and pore volume characteristics for the different Titania materials were measured by a Thermoquest analyzer. Pore specific volume was calculated by using the B.E.T. equation ($C = 12.3839$); whereas, cumulative pore volume was determined by using the B.J.H. equation ($C = 0.8$). The TG/DSC analysis was carried out in an STA 409C of NETZSCH-Gerätebau GmbH Thermal Analysis. The samples were heated from the room temperature up to 1000 °C with a heating rate of 5 °C min⁻¹ under air atmosphere. After the thermal treatment, further XRD analyses were carried out on all the powders. TEM analysis of the various Titania powders was carried out with a Philips CM12 microscope.

2.2 Photoelectrochemical and optical characterization

For optical and photoelectrochemical measurements, the TiO₂ photo-electrodes were prepared by spraying solutions of TiO₂ nanoparticles dispersed in water and isopropyl alcohol onto TCO (19 Ω /sq.) substrates (SnO:F). Before use, TCO glasses were treated for 5 min in an ultrasonic bath of isopropyl alcohol and rinsed with acetone. Triton X-100 was added as dispersant. The coated electrode was dried at 70 °C onto a hot plate and then annealed in an oven at 450 °C for 30 minutes in air. The optical absorption properties were investigated in the absorbance mode with a Hitachi double beam U-3410 spectrophotometer in order to evaluate the energy gap of the thin film semiconductors. The TiO₂ powder deposited (1 cm²) on to conductive FTO and sintered at 450 °C was used as photoanode in the photoelectrolysis half-cell, a glassy carbon disk was used as counter electrode, the reference electrode was Hg/HgSO₄, a 0.5 M H₂SO₄ solution was used as electrolytic solution. The solution was de-aerated with He. The electrochemical apparatus consisted of a Metrohm Autolab potentiostat/galvanostat equipped with a Frequency Responce Analyser (FRA). An Osram solar lamp (300 W) placed at 16 cm distance from the photoanode provided an intensity of illumination of 100 mW cm⁻².

3. RESULTS AND DISCUSSION

3.1 Physico-chemical characterization

Excluding light elements, no relevant amount pollutants was detected by XRF in the powders. However, a small amount of sulphur (~0.5 %) was observed in T-37. A comparison of the

concentration of light elements i.e. CHNS in the various TiO₂ powders is reported in Table 1. The Riedel (R-H) powder showed the lowest amount of organic compounds. Only a very low percentage of carbon was present in this sample and this was in agreement with the TGA results (see below).

Table 1. Contents of light elements in the semiconductor powders.

Sample	C	H	N	S	TOT
P25	1.05%	/	/	/	1.05%
R-H	0.32%	/	/	/	0.32%
T-37	4.70%	1.20%	/	0.75%	6.65%
TO	2.50%	/	/	/	2.50%

The TiO₂ Degussa P25 powder showed an amount of carbon close to 1%. Part of it may be due to the adventitious carbon adsorbed from the atmosphere. The TO powder showed a certain percentage of carbon residues (about 2.5%). The T-37 showed the most relevant presence of C, H and S. The organic content was about 4.7%. This organic content is possibly due to organic residues of the sol-gel preparation process.

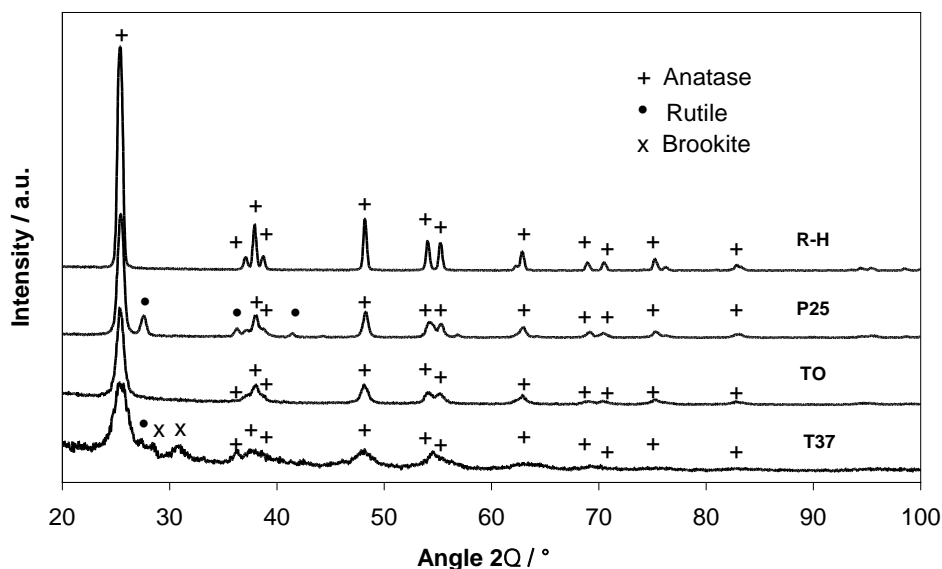


Figure 1. X-ray diffraction patterns of raw TiO₂ powders.

XRD analysis on the TiO₂ nanopowders showed mainly the formation of an anatase phase. For all powders, the main characteristic peak at 25.4° two theta was assigned to the (101) Miller index of anatase. The diffraction pattern of the TiO₂ R-H commercial powder (Fig. 1) shows the characteristic peaks of the anatase structure (JCPDS schedule: 21-1272). No other TiO₂ phase was found in this sample. The mean crystallite size for the R-H powder was about 25 nm. TiO₂ Degussa P25 commercial powder (Fig. 1) showed the peaks of the anatase structure (JCPDS schedule: 21-1272) together with

the rutile structure (JCPDS schedule: 21-1276); this powder is formed by about 85% of anatase and about 15% rutile. The mean crystallite size for this sample related to the anatase structure was about 19 nm.

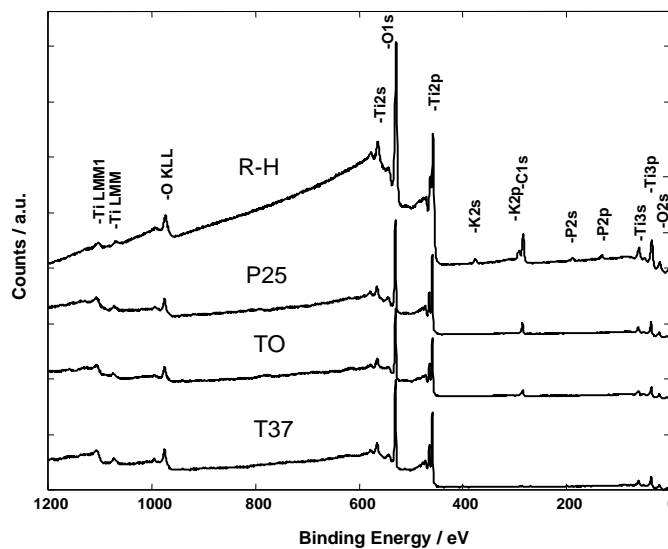


Figure 2. XPS survey spectra of raw TiO₂ powders.

The R-H powder showed the presence of Ti, O, C, and a small amount of P and K on the surface. The latter elements were also detected after an etching process by bombarding with Ar ions the surface (not shown). The P25 showed a high degree of surface chemical purity.

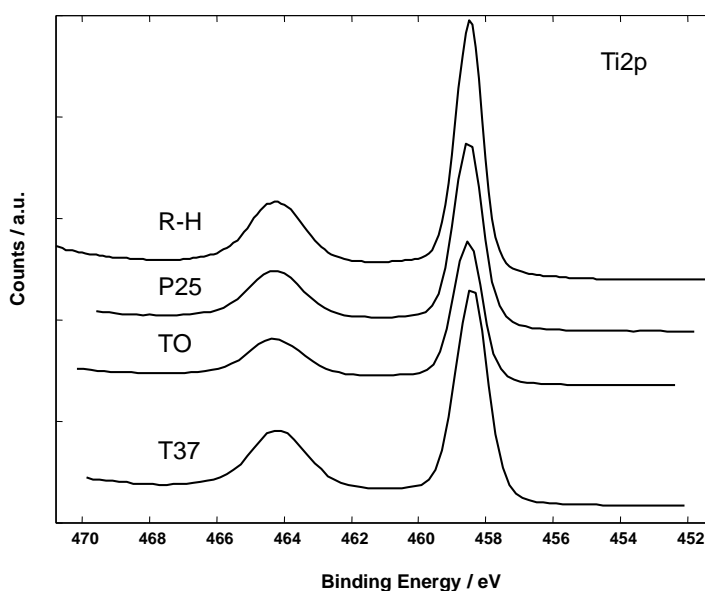


Figure 3. High resolution Ti2p spectra of raw TiO₂ powders.

The diffraction pattern of the TO powder (Fig. 1), obtained by gel combustion synthesis, showed the characteristic peaks of the anatase structure only. The average particle size calculated for this sample was about 12.8 nm. T-37 powder (Fig. 1) obtained by sol-gel synthesis, showed the peaks of the anatase structure (JCPDS schedule: 21-1272), brookite structure (JCPDS schedule: 16-617) and rutile structure (JCPDS schedule: 21-1276). The average crystallite size for this sample related to the anatase structure was about 6 nm.

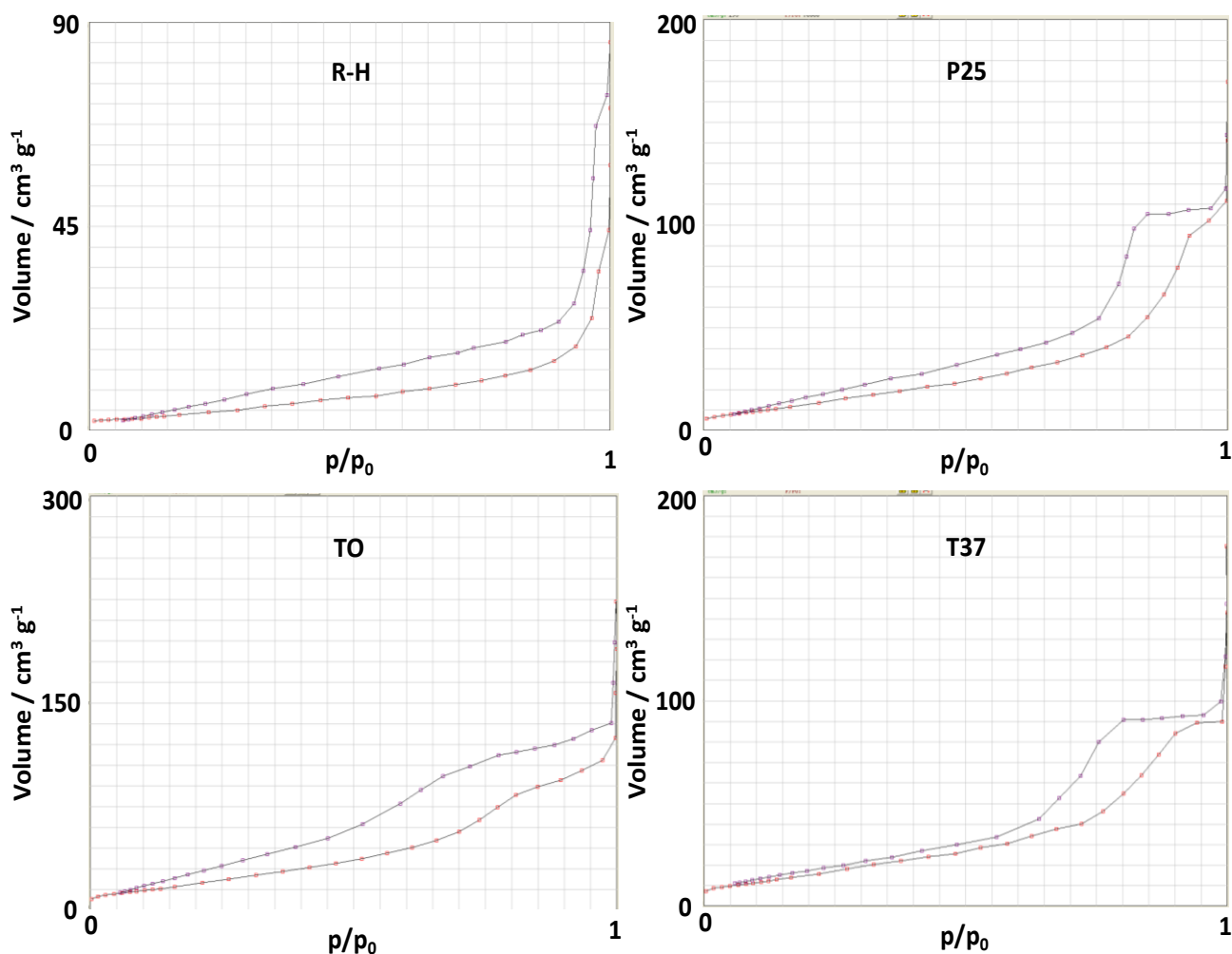


Figure 4. Adsorption-desorption isotherms of raw TiO_2 powders.

The surface chemical composition of the TiO_2 powders was investigated by XPS. The survey spectra of the various TiO_2 samples are compared in Fig. 2.

High resolution XP spectra of the $\text{Ti}2p$ doublet, $\text{Ti}2p_{3/2}$ and $\text{Ti}2p_{1/2}$, are shown in Fig. 3 for the various samples. The binding energy difference, $\Delta E = B.E.(\text{Ti}2p_{1/2}) - B.E.(\text{Ti}2p_{3/2})$, was about 5.6 eV in these samples. The doublet is composed of two symmetric peaks at B.E. of about ($\text{Ti}2p_{3/2}$): 458.6 eV and B.E. ($\text{Ti}2p_{1/2}$): 464.2 eV with intensity ratio about 3:2 as predicted from the theory for this spin-orbit coupling. The doublet was essentially assigned to Ti(IV) (titanium in the IV oxidation state). No clear evidence of Ti (II) and Ti (III) species was observed [27]. However, it is evidenced that the $\text{Ti}2p$

doublet of the T37 sample, characterised by the largest surface area and the smallest particle size, is slightly shifted to lower binding energies probably due to the occurrence of a large number of grain boundary defects sometime associated to sub-stoichiometric sites. In the other samples, it was not envisaged any significant difference.

One of the most common and recognized method of morphology analysis is the Brunauer-Emmett-Teller (BET) model that uses standard gas phase N₂ adsorption isotherms to estimate the surface area and the extent of porosity [28]. Nitrogen adsorption and desorption isotherms for these materials are shown in Fig. 4.

All samples showed two hysteresis loops, indicating that TiO₂ powders consist of a bimodal pore size distribution in the meso-porous region. The shape of hysteresis loops for T37 powder was different than in the other samples. The isotherms of P25, R-H, TO showed H₃-like loops which correspond to the occurrence of slit shape pores, with the possibility of occurrence of micro-pores. The isotherm loop of T37 powder (Fig. 4) showed a steep change in the middle of the desorption branch similar to an H₂-like loop [28]; it is inferred that TiO₂ T37 powder is composed essentially of micro-pores with narrow necks and wider bodies (ink-bottle pores) [28].

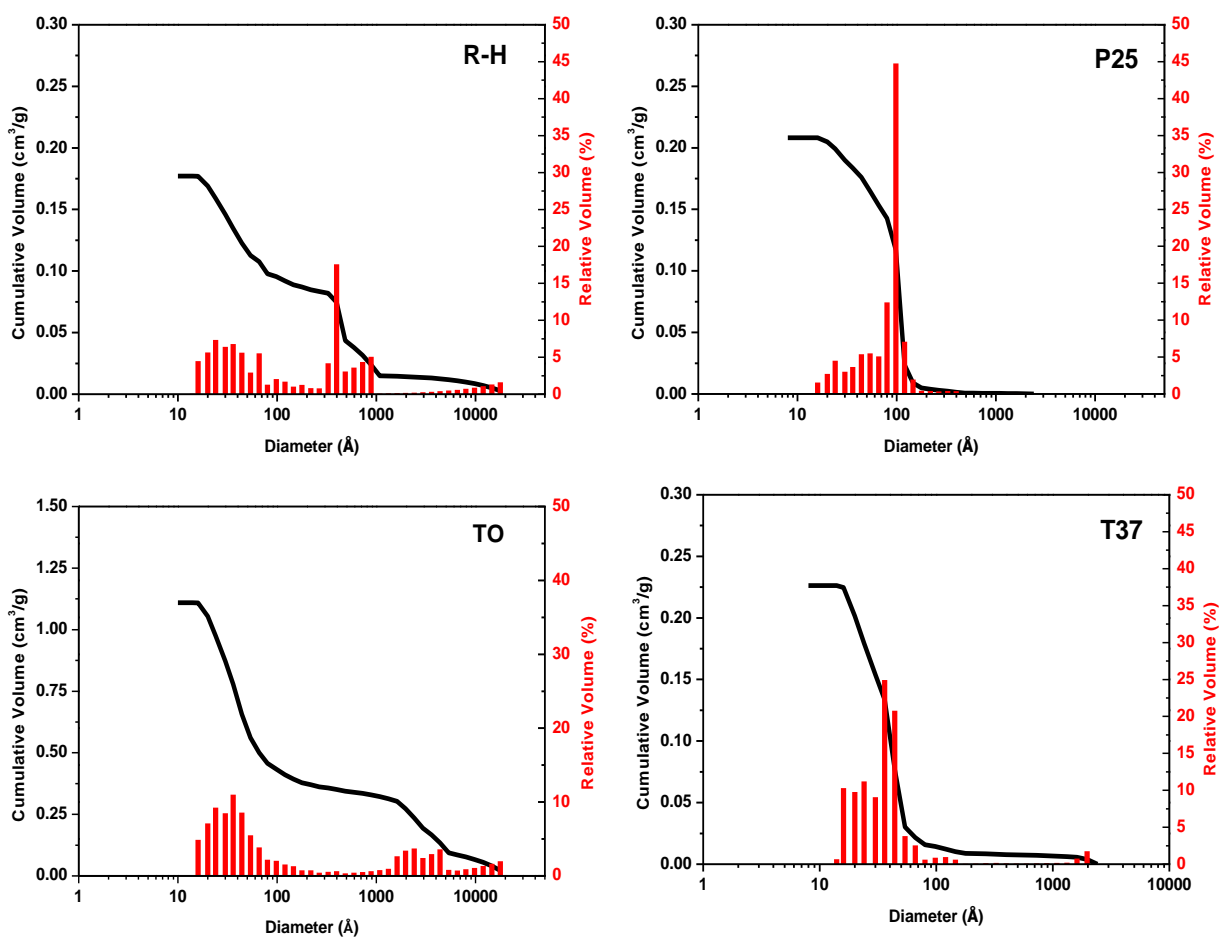


Figure 5. Cumulative and pore volume distribution for raw TiO₂ powders.

Figure 5 shows the pore size distribution curves calculated from the desorption branch of nitrogen isotherm by the BJH method using the Halsey equation [29]. It could be observed that all the samples showed trimodal pore size distributions consisting of micro-pores (<2 nm), small mesoporous (about 3 nm) and large mesoporous (about 50 nm). Micro-pores came from the intra-aggregated pores formed among poorly crystalline TiO₂ particles. According to Kumer et al. [28], a bimodal pore size distribution in meso-pore region can be due to the occurrence of hard aggregates in the powders. Small meso-pores (represented by the hysteresis loop in the lower p/p_0 range from 0.4 to 0.7) are possibly due to the finer intra-aggregated pores formed between TiO₂ grains or primary particles and large meso-pores. The latter are essentially the larger inter-aggregated pores (hysteresis loop in the higher p/p_0 range from 0.8 to 1.0). P25 showed (Fig. 5) both micro (<25 Å) and meso (25<d<500 Å) pores. Major contribution is due to pores with about 100 Å of diameter. Accordingly, this powder is mainly mesoporous. The surface area and pore volume were high for T37. There was mainly the occurrence of micro pores in this sample characterised by a large contents of organic material as shown by the elemental analysis. A little amount of macropores was evident but these do not have any relevant influence in determining the cumulative volume in this case. The R-H titania powder showed a meso-porous morphology with small, medium and large pores. The TO sample showed a very important contribution to cumulative volume by meso-pores (from 20 to 50 Å) and a smaller contribution by macro-pores. The surface area and pores volume for the titania powder studied here are reported in Table 2.

Table 2. BET surface area, cumulative pore volume and mean crystallite size for the as prepared samples and after a thermal treatment in air at 450 °C.

Titania Powder	Thermal treatment	Surface Area (m ² /gr)	Pore Volume (gr/cm ³)	Mean crystallite size from XRD
P25	raw	68.5	0.221	19
P25(450)	450 °C	45.28	0.172	22
RH	raw	21	0.08	25
RH(450)	450 °C	13.89	0.06	25
T37	raw	201.93	0.99	6
T37(450)	450 °C	58.6	0.18	13
TO	raw	127.46	0.53	13
TO(450)	450 °C	68.04	0.24	17

It appears that both the surface area and pore volume show the same trend observed for the crystallite size in these materials. The TGA allowed to determine the weight loss e.g. due to water desorption and combustion of organic components in the TiO₂ powders. DSC measurements were carried out to analyze the phase transitions and exothermic and endothermic modifications occurring during the temperature sweep. Thermal analyses of the as-synthesized TiO₂ nano-powders are reported in Fig. 6. The R-H powder (Fig. 6) showed the smallest amount of organic residues. By

varying the temperature from 20° to 1000 °C, a slight mass loss was observed (about 1%). The large exothermic peak at about 300 °C was probably due to the combustion of the small amount of carbonaceous residues according to the CHNS analysis. A large exothermic peak, starting at about 700 °C, was ascribed to the onset of the modification of anatase phase into rutile. This was confirmed by XRD analysis of this sample after thermal treatment at 1000 °C (Fig. 7). The R-H titania appeared as a very stable material. As an example, the calculated average crystallite size, determined by the Debye Sherrer equation, was still 25 nm after the treatment at 450 °C (Table 2).

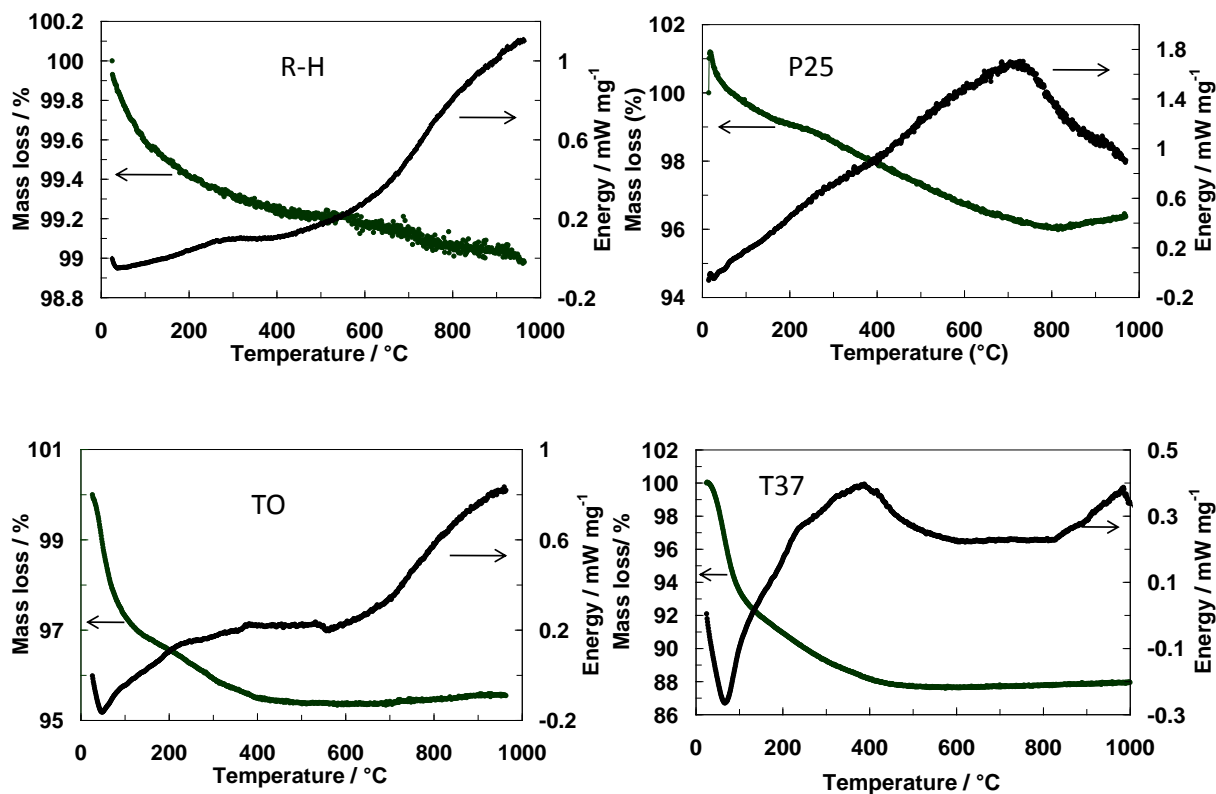


Figure 6. Thermal analysis (DSC-TG) of raw TiO₂ powders.

For P25 sample (Fig. 6), a slight mass loss was observed (about 5%) in the temperature range up to 1000 °C. Until 180 °C the mass loss was due to evaporation of physically adsorbed water on the powder. From 180 °C until about 420 °C the mass loss was probably due to the combustion of organic components (i.e. carbonaceous residues and adventitious carbon). A little presence of carbonaceous components in P25 was confirmed by CHNS analysis as shown above. The mass loss above 420 °C was probably due to the removal of surface hydroxyl groups. The DSC curve showed several peaks: the endothermic one, at about 150 °C, corresponding to the evaporation of adsorbed water, a first exothermic peak between 300° and 400 °C corresponding to the crystallization of anatase and to the combustion of carbonaceous residues; a second peak, in the range between 500° and 600 °C ascribed to the removal of surface hydroxyl groups and a third one at 700 °C corresponding to the onset of anatase-rutile transformation. This transformation appears to reach the completeness at 900-950 °C as

shown by the presence of a well defined peak. Moreover, XRD analysis, carried out after a thermal treatment at 950 °C, confirmed the total transformation of the anatase phases into rutile (Fig. 7).

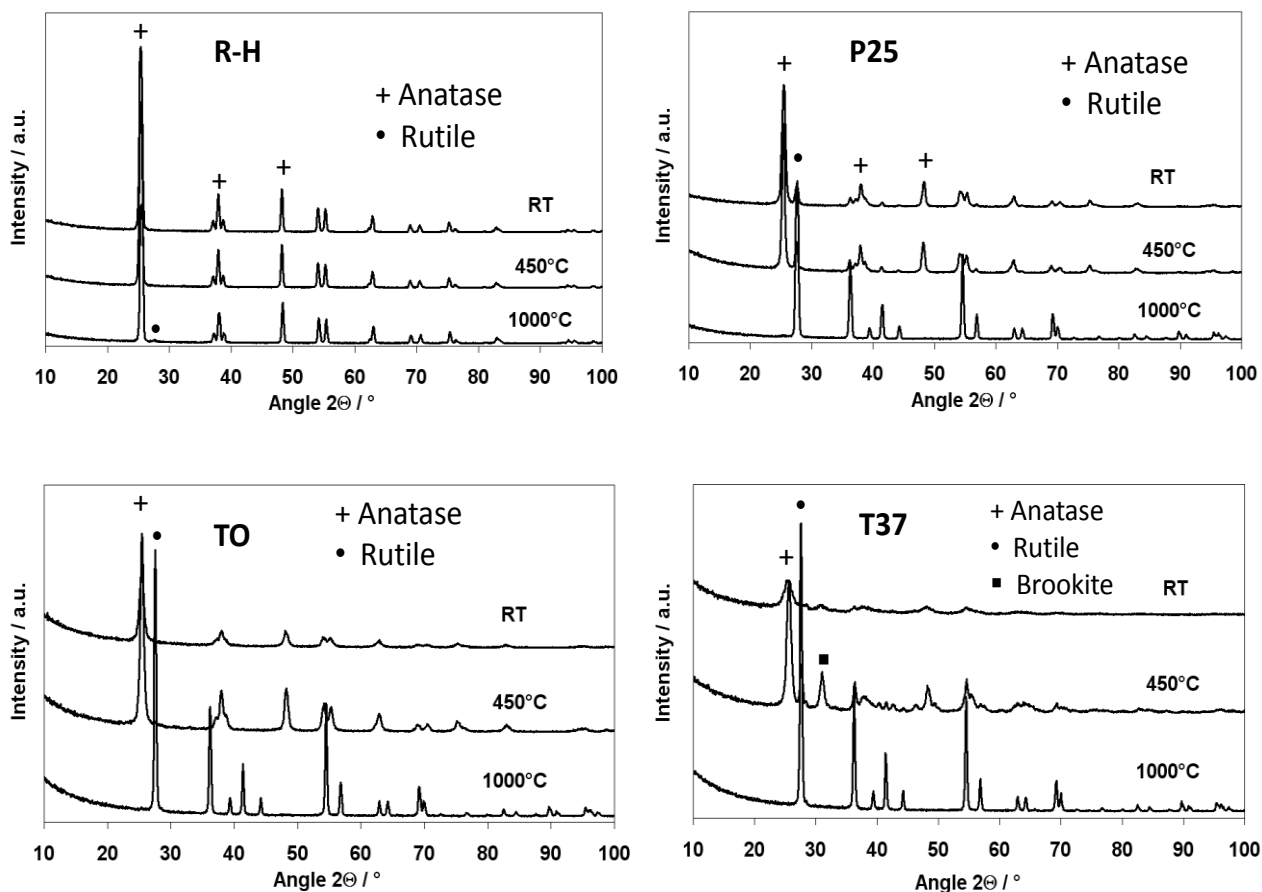


Figure 7. X-ray diffraction patterns of raw and thermal treated TiO_2 powders.

For T-37 powder (Fig. 6), a significant mass loss was observed; about 6% of this loss was due to evaporation of physically adsorbed water on the powder. Another 6.6% of mass loss was due to the combustion of organic components (carbonaceous residues) present in the sample. The DSC curve showed four peaks: an endothermic one, at about 90 °C, corresponding to the evaporation of adsorbed water; the exothermic one at about 280 °C corresponding to the combustion of carbonaceous residues; the peak at 400 °C due to the crystallization of anatase and the third one, with an onset at 600° related to the transformation anatase-rutile that appeared complete at 950°C. All these interpretations were corroborated by XRD analyses (Fig.7)

For the TO powder (Fig. 6), thermo-gravimetric analysis showed a limited weight loss (3%), due to evaporation of physically adsorbed water and another 1.5% loss until 400°C due to the combustion of carbonaceous residues. DSC curve showed four peaks whose interpretation is similar to that of the T37 sample as also confirmed by XRD. All parameters related to crystallographic changes during thermal analysis are summarized in Table 3.

Table 3. Crystallographic phases and crystallite size for the as prepared samples and after thermal treatments in air at 450 °C and 1000 °C.

Thermal treatment	P25	RH	T37	TO
Crystallite size				
Raw	19	25	6	13
450°C	22	25	13	17
1000 °C	-	26	-	-
Phase				
Raw	Anatase/Rutile	Anatase	Anatase/Rutile/Brookite	Anatase
450°C	Anatase/Rutile	Anatase	Anatase/Rutile	Anatase/Rutile
1000 °C	Rutile	Anatase	Rutile	Rutile

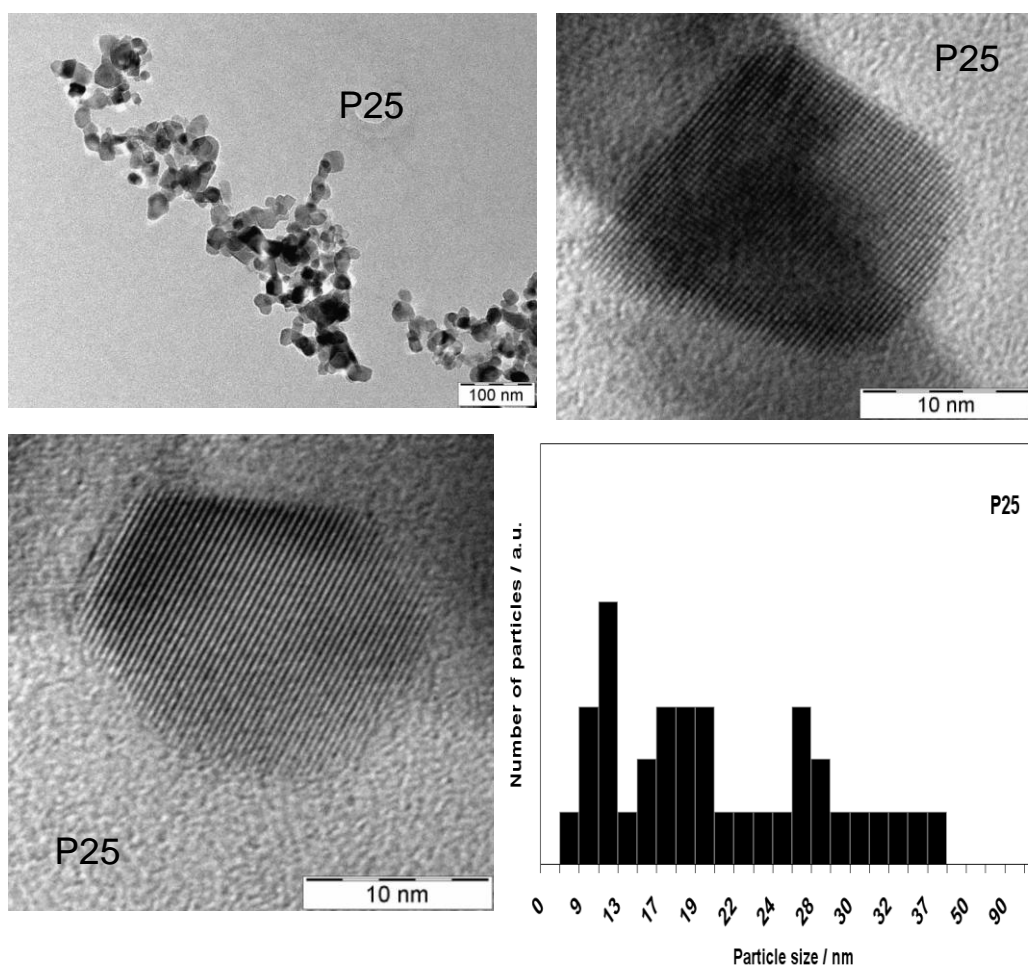


Figure 8. TEM micrographs and particle size distribution for R-H TiO₂.

TEM images are presented in Fig. 8-11 at different magnifications. TEM images of P25, R-H and TO powders showed that these samples were composed of nanosized crystallites with well defined crystallite shapes, although those of the TO sample appeared slightly irregular. High resolution TEM analysis confirmed that the crystallites in these three samples were mainly present as primary particles.

Different was the situation for the sample T 37 that showed essentially particle agglomerates. TEM images of the P25 sample (Fig. 8) showed spherical, elongated and polygonal particles with sizes ranging from 7 to 37 nm. The crystallites in this commercial sample were present in two different phases, i.e. anatase and rutile phases. The particle size distribution was consistent from TEM with the average crystallite sizes for the anatase (19 nm) crystallites from XRD calculated according to the Scherrer equation.

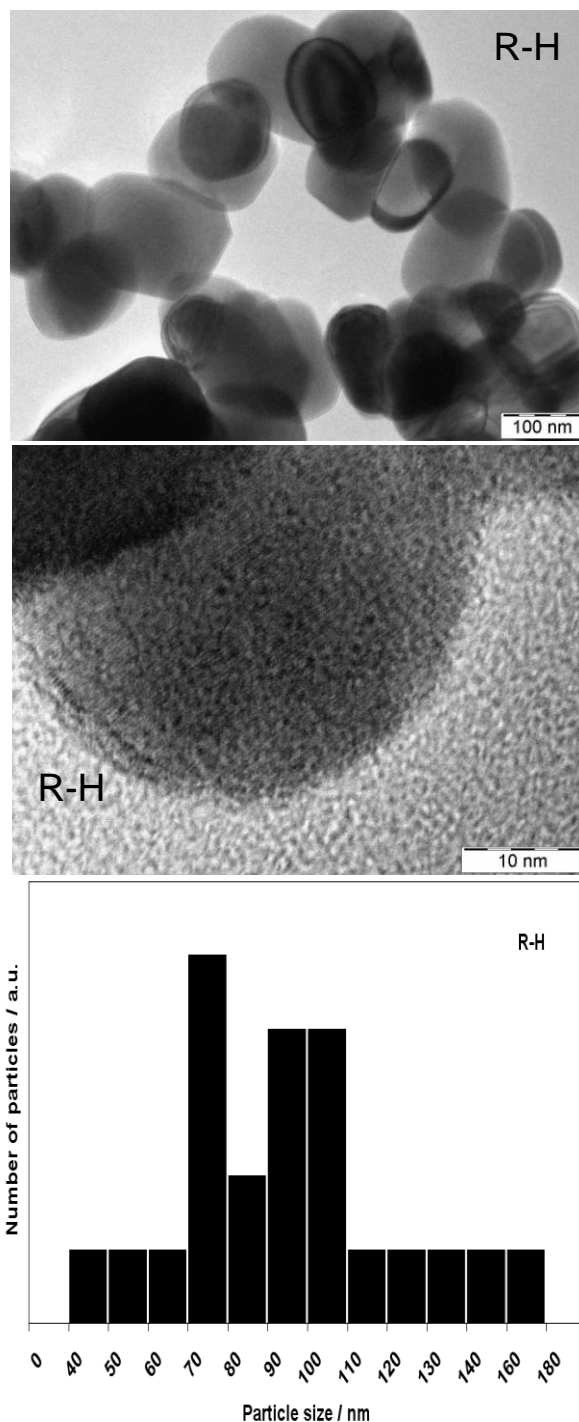


Figure 9. TEM micrographs and particle size distribution for P25 TiO₂.

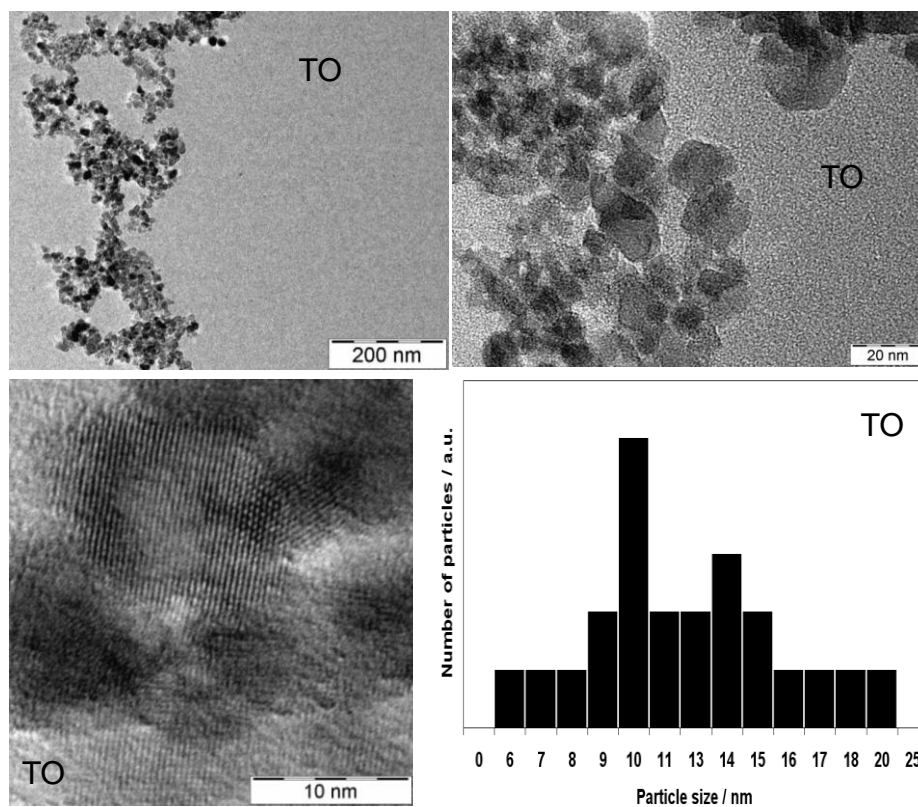


Figure 10. TEM micrographs and particle size distribution for TO TiO₂.

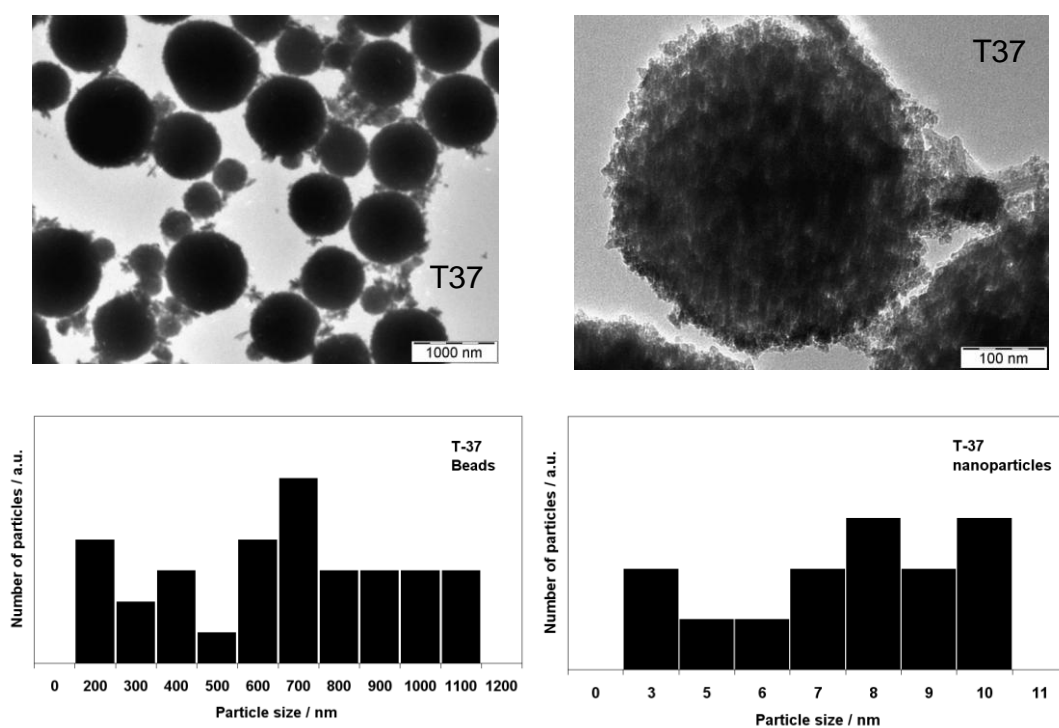


Figure 11. TEM micrographs and particle size distribution for T37 TiO₂.

The R-H sample (Fig. 9) showed well defined round particles consisting only of the anatase phase. Most of the particles in this sample have dimensions within 70-100 nm range which are significantly larger than the crystalline domain size determined by XRD (25 nm). It appears that the agglomeration hinders to individuate all the small particles present in the sample from TEM analysis. Whereas, all crystalline domains contribute to peak broadening in XRD. TEM images of the TO sample (Fig. 10) showed irregularly spherical particles with probably very thin amorphous layers of titanium oxide on the surface. The average particle size 9-15 nm is compatible with the value determined by XRD (13 nm). The morphology of the T37 powder (Fig. 11) showed a strong difference with respect to all other powders. It was envisaged the occurrence of roughly compact spherical agglomerates (about 0.5 - 1 micrometer) similar to beads. As illustrated in the high magnification TEM image, these TiO₂ beads contained nanocrystals (up to 10 nm) and several pores could be observed over the surface of the beads. Furthermore, the presence of some rods close to the beads possibly due to the occurrence of rutile and brookite phases is observed.

3.2 Optical and photoelectrochemical characterization

Photo-electrochemical properties of the Titania powders were investigated in a photo-electrolysis half cell. This is a very simple device consisting of the TiO₂ photoanode as working electrode, a reference electrode and a counter electrode all immersed in water. O₂ evolution occurs at the photoanode and H₂ evolution at the counter electrode. The presence of the reference electrode allowed to get information on the Titania electrode/electrolyte interface only. Since the aim of the work was to compare the characteristics of the powders prepared by different routes, no specific modification of Titania powders was made e.g. in terms of doping, surface treatment with reaction promoters etc. as required to achieve useful conversion efficiencies. If one excludes a thermal sintering at 450 °C as necessary to stabilize the adhesion of the photoelectrode film to the substrate and the continuity of the TiO₂ network in the electrode layer, the powders were essentially investigated in the bare form. The objective was to compare the photoelectrochemical properties of the pure powder in a device less complex than a DSSC cell to correlate its solar conversion characteristics with the physico-chemical properties. It is important to remember that an undoped Titania due to its wide energy gap essentially absorbs only a small fraction of the solar spectrum in the UV region.

Since the optical properties are of relevant interest for these applications, a specific analysis of the absorbance characteristics in the UV-Vis-NIR regions was carried out (Fig.12). It is evident in the absorption spectra the occurrence of a strong absorption onset below 400 nm associated with the direct transition and a shoulder at larger wavelengths. The latter is associated to a possible indirect transition as a consequence of crystallographic impurities [30,31] as well as due to the absorption induced by electronic states in the energy gap. The largest absorption at higher wavelengths is shown by the T37 sample that contains brookite [31] as well as the largest number of organic impurities, whereas the RH sample also shows a significant absorption at intermediate wavelengths (750 nm) possibly due to the indirect transition. The latter is also present in the P25 but shifted at lower wavelengths (550 nm).

Interestingly, the powder prepared by gel combustion shows the lowest level of absorption states at wavelengths larger than those related to the direct transition.

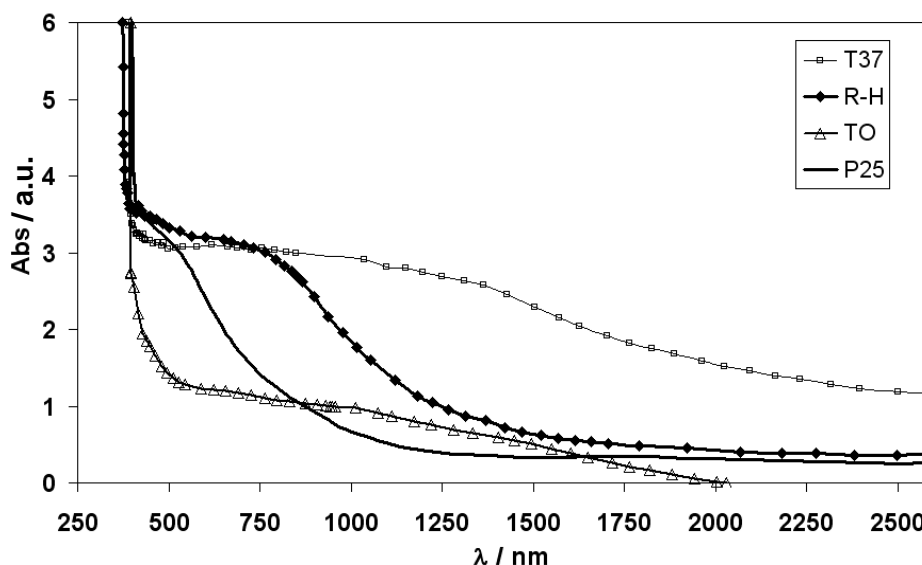


Figure 12. Optical absorption spectra of the various TiO₂ samples.

However, the shoulder is broadened as compared to P25. This may be due to a wide distribution of the electronic levels associated to the impurities in the band gap. The optical band gap, E_g , was obtained from the absorption coefficient measurements using the well known Tauc's formula:

$$\alpha h\nu = \text{const.} \cdot (h\nu - E_g)^n$$

where α is the absorption coefficient, and n is equal to 0.5 for allowed direct transitions and 2 for indirect transitions. In Fig. 13, $(\alpha h\nu)^2$ versus $h\nu$ shows a linear relationship, indicating a main direct transition for all titanium dioxide samples. The intercept on the photon energy axis is equal to the direct band gap, E_g , for each material. This corresponds to 3.25 eV for RH, 3.1 eV for P25, 3 eV for T37, 2.8 eV for TO. This trend does not reflect specifically any physical property. In general, a decrease of the particle size may cause a decrease of the E_g possibly due to the increase of defects and grain boundaries concentration that causes the occurrence of electronic levels bridging the edges of valence and conduction bands. However, the T37 sample characterised by the smallest particle size shows an E_g larger than the TO powder. The latter shows some amorphous-like layer on the surface (Fig. 10).

When a semiconductor (SC) is brought into contact with the electrolyte, consisting of a redox couple such as the H₂O/O₂, a depletion of majority charge carriers (n-type in TiO₂) across the interface takes place on account of the difference in the chemical potentials of the two phases. This results in a band bending in the semiconductor near the interface. The irradiation of the semiconductor

electrode produces a change in the electrode potential due to the generation of electron hole pairs followed by their separation under the electric field across the depletion region.

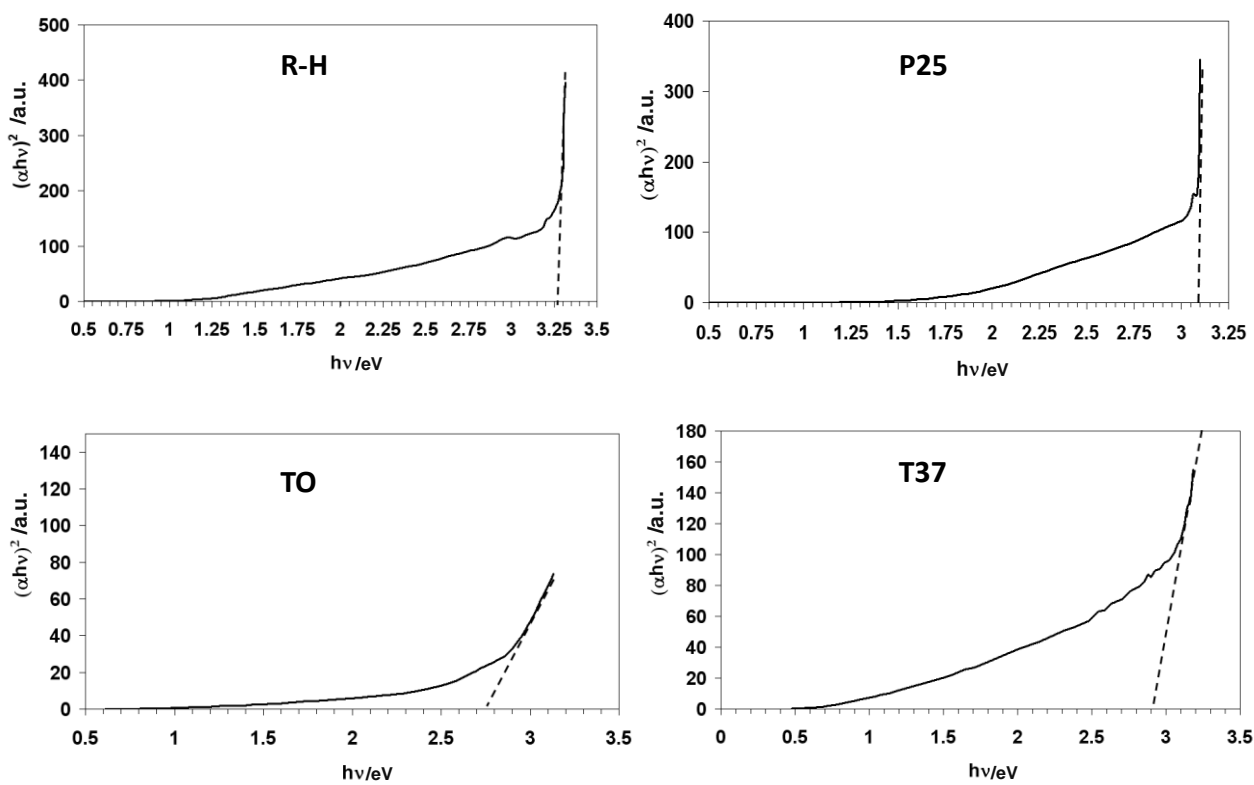


Figure 13. Direct transition energy gap plots of the various TiO₂ samples.

Under illumination and open circuit condition, the accumulation of photo-generated charge carriers across depletion region reduces the band bending. Thus, the behaviour of an electrode-electrolyte junction can be investigated by measuring the current-voltage (I-V) characteristics. The I-V characteristic of the photoelectrodes under investigation is shown in Fig. 14. The I-V response is reported under illumination only; the dark current was quite low in the region of technical interest and similar for all materials.

For a n-TiO₂ (large band gap semiconductor) the equilibrium concentration of holes is extremely low and the anodic dark current, determined by diffusion of holes towards the surface, is, in accordance, very low. On the other hand, illumination by light ($h\nu > E_g$) leads to a generation of electron-hole pairs, which are separated by the electric field within the space charge region. The holes coming towards the surface get consumed in the electrochemical oxidation reaction. While electrons forced towards the interior move through the electrical circuit and take part in the counter electrochemical reaction (i.e. reduction). In the present case, the measured photocurrent response (Fig. 14) corresponds to oxygen evolution (oxidation of water) at the TiO₂ electrode surface.

Accordingly, upon irradiation, a photocurrent was observed at potentials quite negative with respect to the redox potential of water in acid electrolyte ~ 1.23 V (RHE). This was due to the fact that some of the energy required for the oxidation of water to O₂ was provided by the radiation (via the

high energy holes) and the process occurs under conditions much more favourable than the thermodynamic condition for oxygen evolution in the dark $E > 1.23$ V (RHE).

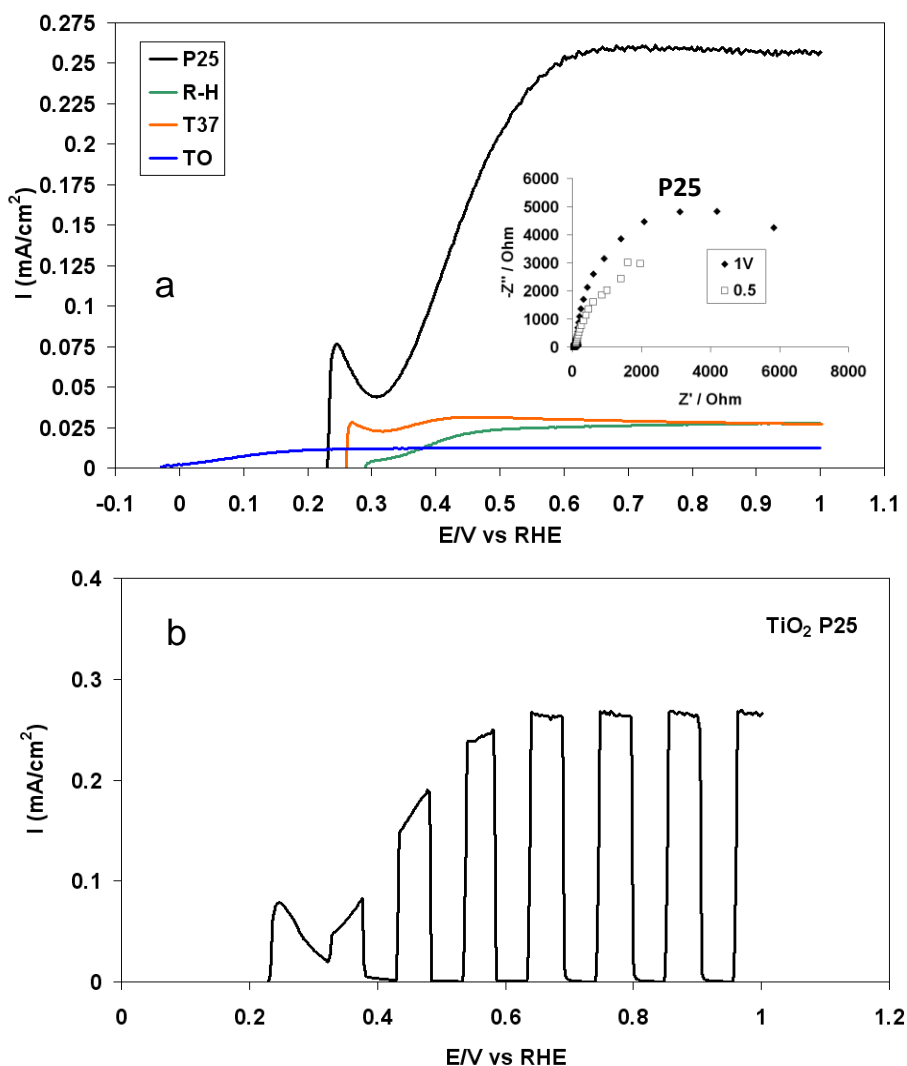


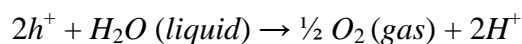
Figure 14. a) Photocurrent vs. potential curves for oxygen evolution at the TiO₂ electrolyte interface. The inset shows the corresponding ac-impedance plot for P25. b) Chopped light response for the TiO₂ P25 sample for the oxygen evolution at the TiO₂ electrolyte interface.

As mentioned above, light absorption results in intrinsic ionization of the n-type semiconductor over the band gap, leading to the formation of in the conduction band electrons and holes in the valence band:



This process takes place when the energy of photons ($h\nu$) is equal to or larger than the band gap. The electric field at the electrode/electrolyte interface avoids recombination of the

photogenerated charge carriers. Thus, the light-induced electron-hole pairs result in the splitting of water molecules into gaseous oxygen and hydrogen ions at the TiO₂-electrolyte interface:



The onset potential of photocurrent is negatively shifted vs. the reversible potential by about 1 V for most of the TiO₂ powders and about 1.25 V for the TO powder with respect to the reversible potential in the dark i.e. 1.23 V RHE. A pre-peak is especially observed for the materials which showed a clear evidence of absorption at wavelengths larger than 400 nm in the optical absorption spectra. As above discussed, this was attributed to the occurrence of electronic levels within the band gap. From the optical spectra, the TO powder was the material showing the smallest contribution from these energy level or from an indirect transition to the optical properties. The photocurrent response in Fig. 14 of this sample did not show a clear pre-peak as the other samples; at the same time, the TO photo-electrode was characterised by the largest photo-potential. Probably, this is essentially caused by the prevailing contribution of the direct transition which is associated to a large energy gap with respect to the occurrence of an indirect transition. Moreover, the presence of widely distributed electronic levels in this sample (Fig. 13) causes recombination and trapping effects for the photogenerated carriers determining low photocurrents. The photocurrent obtained for the P25 photo-electrode was significantly higher than the other TiO₂ semiconductors (Fig. 14). This can not be explained with the presence of a fraction of rutile phase in this material since also the T37 contains a small amount of rutile. The P25 is indeed characterised by good purity both in terms of bulk and surface. The RH powder has a good purity in terms of organic content but the occurrence of K and P surface impurities was detected by XPS. Yet, it appears that the main drawback for the RH with respect to the P 25 sample is the lower surface area (21 vs. 69 m² g⁻¹) and the larger crystallite size. This determines the occurrence of a lower number of active surface sites for the oxygen evolution in the RH sample with respect to P25. Whereas, in the case of T37, the presence of a large number of impurities with an associated large number of electronic levels in the band gap, as observed from the optical absorption spectra, compensates the positive effect of large surface area (202 m² g⁻¹). Moreover, the sample is mainly microporous, and characterised by large agglomeration than the other samples which are essentially mesoporous. Although the values of photocurrent obtained in the present study are lower than those reported in the literature [32-35], it is pointed out that the present results are reached in an acidic electrolyte, whereas most of the published works deals with alkaline electrolyte, in which water splitting is a faster reaction.

Analysis of impedance spectra (inset) showed a similar series resistance for all photoelectrodes that was much lower than the charge transfer resistance. This indicates that the ohmic contribution was minimal and did not vary much among the different photoelectrodes. Whereas, polarization resistance associated to the charge transfer at the electrode-electrolyte interface and the charge transport in the space charge region is dominant.

4. CONCLUSION

Physical-chemical analysis of the in house prepared and commercial TiO₂ powders showed that most of the powders have a very low amount of inorganic contamination (essentially S, P and K). But there are in some case significant organic residues as resulting from the preparation process. All powders show anatase phase as the main crystalline structure. A certain amount of rutile was observed in the TiO₂ Degussa P25 powder as well as in the TiO₂ powder prepared by sol-gel. A small occurrence of a brookite phase was also detected in this sample. Crystallite sizes for all different powders were ranging from 6 to 25 nm with the sample prepared by sol-gel showing the smallest primary crystallite size. Both BET surface area, cumulative pore volume followed the same trend of the crystallite size in the various samples. The morphology of the sol-gel prepared sample showed the occurrence of spherical agglomerates composed of nanosized primary particles, whereas the other samples showed polygonal, or irregularly spherical single crystals. The sample characterised by the largest primary particle size, i.e. R-H, was the most thermodynamically stable.

The results obtained for the photoelectrolysis cells showed a photocurrent response for all the investigated nano-structured TiO₂ powders consisting of different morphologies even in the absence of specific dopants and surface promoters. The oxygen evolution appears to depend on the intrinsic photo-anode powder properties, including morphology, defect density and optical absorption characteristics. The photo-currents obtained with these materials and in this process are of course much lower than those achieved in DSSC cells because photogenerated electron-hole pairs are only those formed in the TiO₂ space charge layer and the absorbed light is just a small fraction of the solar spectrum radiation (UV region below 400 nm). In addition, another limiting step is represented by the fact that kinetic overpotentials for water splitting are generally quite high for non noble metals and oxides.

The results clearly demonstrate that the photocurrent characteristics are strongly dependent on the chemical purity, crystallite size, porosity and morphology of the TiO₂ photo-electrodes and such evidences suggest the importance of controlling all these material properties for optimizing performance in photo-electrochemical applications.

ACKNOWLEDGEMENTS

The authors gratefully acknowledge the financial support from Tozzi Renewable Energy during the first phase of this study. The research activity is now continuing under the support of the project FOTORIDUCO2 PON01_02257.

References

1. R.L. Hirsch, *Energy Policy*, 36 (2008) 881.
2. N.S. Lewis, *MRS Bull.*, 32 (2007) 808.
3. G.W. Crabtree and N.S. Lewis, *Phys. Today*, 60 (2007) 37.
4. M. Gratzel, *Nature*, 403 (2000) 363.
5. J.H. Yum, P. Chen, M. Grätzel and M.K. Nazeeruddin, *ChemSusChem*, 1 (2008) 699.
6. M. Gratzel, *J. Photochem. and Photobiol. C*, 4 (2003) 145.

7. L. De Marco, M. Manca, R. Giannuzzi, F. Malara, G. Melcarne, G. Ciccarella, I. Zama, R. Cingolani and G. Gigli, *J. Phys. Chem. C*, 114 (2010) 4228.
8. P. Liska, K.R. Thampi, M. Gratzel, D. Bremaud, D. Rudmann, H.M. Upadhyaya and A.N. Tiwari, *Appl. Phys. Lett.*, 88 (2006) 203103.
9. Y. Alivov and Z.Y. Fan, *J. Mater. Sci.*, 11 (2010) 2902.
10. M.K. Nazeeruddin, F. De Angelis, S. Fantacci, A. Selloni, G. Viscardi, P. Liska, S. Ito, B. Takeru and M. Gratzel, *J. Am. Chem. Soc.*, 127 (2005) 16835.
11. J.-Y. Kim, T. Sekino and S.-I. Tanaka, *J. Mater. Sci.*, 46 (2011) 1749.
12. G. Calogero and G. Di Marco, *Solar Energy Materials and Solar Cells*, 92 (2008) 1341.
13. V. Baglio, M. Girolamo, V. Antonucci and A.S. Aricò, *Int. J. Electrochem. Sci.*, 6 (2011) 3375.
14. B. O'Regan and M. Gratzel, *Nature*, 353 (1991) 737.
15. M.K. Nazeeruddin, P. Pechy, T. Renouard, S.M. Zakeeruddin, R. Humphry-Baker, P. Comte, P. Liska, L. Cevey, E. Costa, V. Shklover, L. Spiccia, G.B. Deacon, C.A. Bignozzi and M. Grätzel, *J. Am. Chem. Soc.*, 123 (2001) 1613.
16. T.-H. Tsai, S.-C. Chiang and S.-M. Chen, *Int. J. Electrochem. Sci.*, 6 (2011) 3333.
17. A. Fujishima and K. Honda, *Nature*, 37 (1972) 238.
18. R.A. Kerr, *Science*, 318 (2007) 1230.
19. D.P. Dubal, D.S. Dhawale, A.M. More and C.D. Lokhande, *J. Mater. Sci.*, 46 (2011) 2288.
20. D. Wei and G. Amaratunga, *Int. J. Electrochem. Sci.*, 2 (2007) 897.
21. D. Menzies, Q. Dai, Y.-B. Cheng, G. Simon and L. Spiccia, *J. Mater. Sci.*, 39 (2004) 6361.
22. K. Shankar, G.K. Mor, H.E. Prakasam, S. Yoriya, M. Paulose, O.K. Varghese and C.A. Grimes, *Nanotechnology*, 18 (2007) 065707.
23. T. Denaro, V. Baglio, M. Girolamo, V. Antonucci, A.S. Aricò, F. Matteucci and R. Ornelas, *J. Appl. Electrochem.*, 39 (2009) 2173.
24. A. Arena, N. Donato, G. Saitta, G. Rizzo, G. Neri and G. Pioggia, *J. Sol-Gel Sci. Technol.*, 43 (2007) 41.
25. S.T. Aruna and K.C. Patil, *J. Mat. Synth. Process*, 4 (1996) 175.
26. F.A. Deorsola and D. Vallari, *J. Mater. Sci.* 43 (2008) 3274.
27. J.F. Moulder, W.F. Stickle, P.E. Sobol and K.D. Bomben, *Handbook of X-ray photoelectron spectroscopy*; Physical Electronics Inc. (1995).
28. B.L. Newalkar, N.V. Choudary, U.T. Turaga, R.P. Vijayalakshmi, P. Kumar, S. Komarneni and T.S.G. Bhat, *Microporous Mesoporous Mater.*, 65 (2003) 267.
29. P.J. Pomonis and E.T. Tsaousi, *Langmuir*, 25 (2009) 9986.
30. H.M. Yang, X.C. Zhang and Q.F. Tao, *Inorganic Materials*, 45 (2009) 1139.
31. R. Zallen and M.P. Moret, *Solid State Commun.*, 137 (2006) 154.